# Area-selective atomic layer deposition of metal oxides on noble metals through catalytic oxygen activation

Please check the document version of this publication:

• A submitted manuscript is the version of the article upon submission and before peer-review. There can be important differences between the submitted version and the official published version of record. People interested in the research are advised to contact the author for the final version of the publication, or visit the DOI to the publisher's website.
• The final author version and the galley proof are versions of the publication after peer review.
• The final published version features the final layout of the paper including the volume, issue and page numbers.

Link to publication

# Area-Selective Atomic Layer Deposition of Metal Oxides on Noble Metals through Catalytic Oxygen Activation

Joseph A. Singh,[†,#] Nick F. W. Thissen,[‡,#] Woo-Hee Kim,[§,||] Hannah Johnson,[⊥] Wilhelmus M. M. Kessels,[‡] Ageeth A. Bol,[‡] Stacey F. Bent,*[,||] and Adriaan J. M. Mackus*[,‡,||]

[†]Department of Chemistry, Stanford University, 333 Campus Drive, Stanford, California 94305, United States

[‡]Department of Applied Physics, Eindhoven University of Technology, P.O. Box 513, 5600 MB Eindhoven, Netherlands

[§]Division of Advanced Materials Engineering, Chonbuk National University, 567 Baekje-daero, deokjin-gu, Jeonju-si, Jeollabuk-do, 54896, Republic of Korea

[||]Department of Chemical Engineering, Stanford University, 443 Via Ortega, Stanford, California 94305, United States

[⊥]Advanced Technology 1, Toyota Motor Europe NV/SA, Hoge Wei 33A, B-1930 Zaventem, Belgium

**S** *Supporting Information*

**ABSTRACT:** Area-selective atomic layer deposition (ALD) is envisioned to play a key role in next-generation semiconductor processing and can also provide new opportunities in the field of catalysis. In this work, we developed an approach for the area-selective deposition of metal oxides on noble metals. Using $O_2$ gas as co-reactant, area-selective ALD has been achieved by relying on the catalytic dissociation of the oxygen molecules on the noble metal surface, while no deposition takes place on inert surfaces that do not dissociate oxygen (i.e., $SiO_2$, $Al_2O_3$, Au). The process is demonstrated for selective deposition of iron oxide and nickel oxide on platinum and iridium substrates. Characterization by *in situ* spectroscopic ellipsometry, transmission electron microscopy, scanning Auger electron spectroscopy, and X-ray photoelectron spectroscopy confirms a very high degree of selectivity, with a constant ALD growth rate on the catalytic metal substrates and no deposition on inert substrates, even after 300 ALD cycles. We demonstrate the area-selective ALD approach on planar and patterned substrates and use it to prepare $Pt/Fe_2O_3$ core/shell nanoparticles. Finally, the approach is proposed to be extendable beyond the materials presented here, specifically to other metal oxide ALD processes for which the precursor requires a strong oxidizing agent for growth.
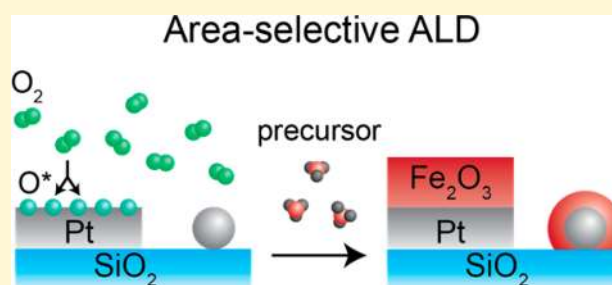
## INTRODUCTION

Area-selective deposition plays an increasingly important role in the development of nanostructured materials for semiconductor processing[1,2] and catalysis.[3,4] In semiconductor processing, conventional fabrication of multilayer device structures is facing the challenge of aligning the layers with nanometer accuracy. Use of area-selective deposition allows for control over where deposition takes place without requiring photolithography for every device layer.[1] Consequently, the number of lithography steps can be reduced, which eliminates these alignment errors while lowering the fabrication costs.

In catalysis, there is a desire to create highly controlled bimetallic or core/shell nanoparticles that are monodisperse and of high purity. Conventional synthetic methods have difficulty ensuring a consistent bimetallic composition.[5−8] Large improvements can be expected if the deposition of the second material occurs selectively on the first material only, and not on the surrounding support substrate. This ensures that all particles are covered uniformly, while preventing the formation of monometallic particles of the second material.

Atomic layer deposition (ALD) utilizes self-limiting reactions of precursor and co-reactant gases to achieve highly controlled deposition. ALD has many favorable attributes including high conformality, good spatial uniformity, and Å-level thickness control. Since the chemical reactions occur only on the substrate surface, area-selective ALD can be achieved by either blocking or activating the growth on specific areas or materials. Prior reports have shown that such selectivity can be obtained by chemically modifying surfaces to prevent growth.[1,2,9−15] Alternatively, ALD growth can be activated on an inert substrate by locally catalyzing the surface reactions of an ALD process.[8,16−18] Etching can be added as part of the area-selective ALD process to improve the selectivity.[19,20]

Prior work has shown that area-selective ALD by area activation can be achieved by choosing a suitable co-reactant.[3,8,16−18,21] For example, a mildly oxidizing co-reactant such as $O_2$ gas may allow for area-selective growth on certain

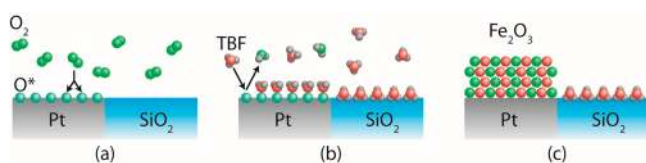surfaces, while more strongly oxidizing co-reactants such as ozone or $O_2$ plasma generally result in growth on any surface and are therefore not suitable for area-selective deposition. Weber et al. used this approach to synthesize Pt/Pd and Pd/Pt core/shell nanoparticles supported on $Al_2O_3$ substrates.[16,18] Selective deposition of Pt on Pd particles was achieved by using $O_2$ gas as the co-reactant. The Pd particles are able to catalyze the surface reactions of subsequent Pt ALD. More specifically, noble metal surfaces catalyze the dehydrogenation and combustion of precursor ligands.[8,16,18,22] The latter is driven by dissociative chemisorption of $O_2$ into $O^*$ (chemisorbed O). These catalytic surface reactions allow for deposition of Pt only on the Pd particles and not on the surrounding $Al_2O_3$ substrate. In a similar way, Pd deposition on Pt particles was enabled by using $H_2$ gas, where this time the Pt particles catalyze the formation of $H^*$ reactive sites. Lu et al. expanded this methodology by exploiting the selective chemisorption of $O_2$ and $H_2$ to synthesize bimetallic PdPt, RuPt, and RuPd nanoparticles on $Al_2O_3$.[8]

In this work, we extend this approach to area-selective ALD of metal oxides by demonstration of selective iron oxide and nickel oxide deposition on catalytic Pt and Ir substrates. We focus particularly on Pt-Fe based materials since this system has key applications in catalysis and magnetic devices. For example, Pt-Fe can be used for carbon nanotube growth,[23−26] the oxygen reduction reaction,[27] and room temperature CO oxidation.[28] Furthermore, the use of ALD to prepare these materials may allow them to be integrated into next-generation catalyst designs[3] and take advantage of ALD's favorable attributes for catalyst synthesis.[3,4,21,29−32] As a result of their magnetic properties, Pt-Fe based materials have key applications for creating memory[33,34] and spintronic devices,[35] and are used in medical imaging.[36]

Area-selective ALD is achieved by exploiting the catalytic activation of $O_2$ on Pt and Ir substrates, which enables deposition of iron oxide and nickel oxide from $t$-butyl ferrocene (TBF) and nickelocene precursors, respectively. These precursors are relatively unreactive and usually require strongly oxidizing co-reactants such as ozone or $O_2$ plasma to combust the ligands and result in deposition.[37,38] However, in this work, we show that deposition can also be achieved with $O_2$ gas when a catalytic substrate such as Pt or Ir is used. On such catalytic metals, $O_2$ gas is catalytically activated through dissociative chemisorption (Figure 1). The reactive $O^*$ species are in this case formed at the catalytic substrate instead of supplied by the ozone or $O_2$ plasma. On the other hand, deposition does not take place on materials such as $SiO_2$, $Al_2O_3$, and Au as these

materials do not dissociate the $O_2$ gas. In this way, by using $O_2$ gas, area-selective deposition is achieved on the catalytic Pt and Ir substrates, while no growth is obtained on noncatalytic substrates such as $SiO_2$. In this mechanism of catalytic dissociation by the substrate metal, one might expect growth of the transition metal oxide to terminate when all the surface Pt or Ir sites are covered by the growing film. However, as shown in this work, we observe sustained growth even after depositing a film of 20 nm in thickness. Two potential mechanisms are proposed to explain these results. Using this process, we successfully synthesize patterned bilayer thin films as well as core/shell nanoparticles.
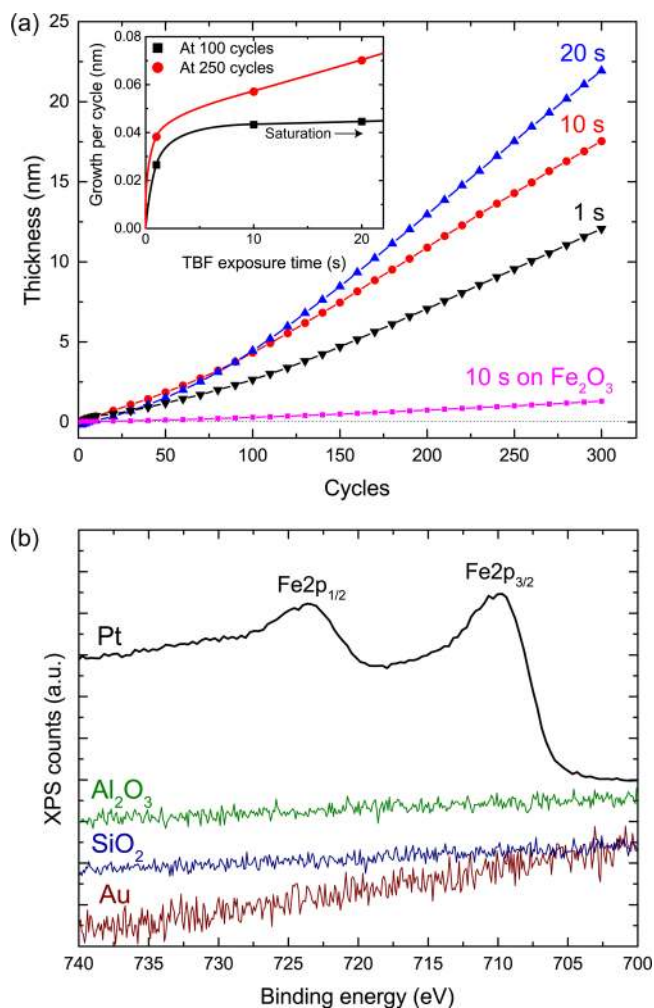
## ■ METHODS

In this work, we performed several processes in three different ALD reactors, located at Eindhoven University of Technology (TU/e) and Stanford University. The TU/e reactor was used for $Fe_2O_3$ film depositions on planar substrates but not on particles. The experiments include $in$ $situ$ spectroscopic ellipsometry (SE) measurements on various substrates (Figure 2a), and deposition on patterned Pt squares (Figure 5). The Stanford reactors were used for $Fe_2O_3$ deposition on supported Pt particles (Figure 6, Figure 7, and Figure S3), and $Fe_2O_3$ and NiO deposition on patterned Ir substrates (Figure S2). We note that the similar results obtained in the TU/e high-vacuum reactor and the Stanford low-vacuum reactors supports the robustness of our approach.

The TU/e reactor is a high-vacuum system that is evacuated by combination of a rotary and a turbomolecular pump to a base pressure of ∼$10^{-6}$ Torr. The system has been extensively described in previous work.[39] $Fe_2O_3$ depositions were performed using $t$-butyl ferrocene precursor (TBF, 98%, Strem Chemicals) and $O_2$ gas. The TBF was kept at 100 °C to ensure adequate vapor pressure and was dosed using an Ar carrier gas through a delivery line heated to 120 °C. Each cycle consisted of 1−20 s TBF exposure (as indicated in the results), 10 s pump time, 10 s $O_2$ exposure, and 10 s pump time. The reactor walls were kept at 100 °C, and the substrate table was heated to 300 °C. Due to poor thermal contact in vacuum, however, the actual temperature of the samples during the process is typically lower.[40] For the area-selective process, a high $O_2$ pressure of 750 mTorr was used to improve the thermal contact, giving a sample temperature of ∼250 °C as measured by spectroscopic ellipsometry (see below).

The Stanford reactors were of two types: a custom-built, low-vacuum system and a commercial Arradiance Gemstar low-vacuum system. Processes were developed for NiO and $Fe_2O_3$ depositions on planar samples using the custom system (Figure S2). Typical oxygen pressures on the order of 1−10 Torr were used. Depositions were performed at a 1 Torr $N_2$ operating pressure. For NiO ALD, the substrates were heated to 250 °C and the nickelocene precursor was heated to 70 °C. Each cycle consisted of 7 s nickelocene exposure, 40 s purge time, 3 s $O_2$ exposure, and 30 s purge time. For $Fe_2O_3$ ALD, the substrates were heated to 225 °C and the TBF precursor was heated to 95 °C. Cycles consisted of 8 s TBF exposure, followed by 10 s holding time, 10 s purge time, 3 s $O_2$ exposure, and 30 s purge time.

The selectivity of the process was checked in the TU/e reactor by $in$ $situ$ SE on five different substrate materials: (1) Pt, (2) Au, (3) $Fe_2O_3$, (4) $SiO_2$. and (5) $Al_2O_3$. These substrates will be referenced in the results, but details are described here. (1) The Pt films were 20 nm in thickness and were deposited by plasma-assisted ALD on thermal $SiO_2$.[41] (2) The Au films were 16 nm in thickness and were deposited by electron-beam evaporation. (3) $Fe_2O_3$ films were ∼5 nm in thickness (without an underlying Pt substrate) and were deposited by plasma-assisted ALD of $Fe_2O_3$ on $SiO_2$, using the process reported by Ramachandran et al.[42] Due to the use of $O_2$ plasma, this is a conventional, nonselective process which allows for deposition on noncatalytic substrates. (4) $SiO_2$ substrates consist of as-received 450 nm thermal $SiO_2$ on Si. (5) The $Al_2O_3$ films (20 nm) were deposited on $SiO_2$ by ALD. The $in$ $situ$ SE measurements were performed using a J.A. Woollam, Inc. M2000 ellipsometer (1.2−5.0 eV photon range).[43]



**Figure 1.** Schematic illustration of the proposed mechanism by which area-selective ALD occurs. As an example, we illustrate $Fe_2O_3$ deposition from $t$-butyl ferrocene (TBF)/$O_2$ on Pt. (a) Pt surfaces allow for the dissociative chemisorption of $O_2$ to $O^*$ (chemisorbed oxygen), whereas $SiO_2$ surfaces do not catalyze this reaction. (b) While TBF adsorption may occur on both surfaces, TBF only fully reacts where $O^*$ is present and therefore only leads to deposition on Pt. (c) In this way, a film of $Fe_2O_3$ can be deposited selectively by ALD on the Pt.

**Figure 2.** (a) Thickness measured by *in situ* SE during deposition of Fe$_2$O$_3$ from TBF/O$_2$ on Pt with various TBF exposure times, with growth on Fe$_2$O$_3$ shown for comparison. Almost negligible growth is observed on the Fe$_2$O$_3$ substrate. (a, inset) Saturation curves showing the growth per cycle of Fe$_2$O$_3$ deposited on Pt substrates, extracted at 100 and at 250 cycles from the *in situ* SE data. The growth per cycle is determined by dividing the thickness at 100 or 250 cycles of deposition by the number of cycles performed. (b) X-ray photoelectron spectroscopy (XPS) scans showing the Fe$_{2p}$ region after 300 ALD cycles of Fe$_2$O$_3$ on Pt, Au, SiO$_2$, and Al$_2$O$_3$ substrates. A clear Fe$_{2p}$ signal is observed on Pt, but no Fe above the detection limit is detected on the catalytically inactive substrates.

Prior to the experiments, the sample temperature was determined by SE. A Si wafer with native oxide was measured using SE for different O$_2$ pressures, and modeled using a J.A. Woollam temperature-sensitive optical model.

For XPS and cross-sectional TEM measurements, planar Fe$_2$O$_3$ films were deposited on electron-beam evaporated Pt films (∼16 nm). Cross-sectional TEM images were obtained at TU/e using a JEOL JEM-ARM200F system. The TEM lamella was cut from the sample by focused ion beam (FIB) milling. Prior to FIB milling, a protective layer of SiO$_2$ was deposited by electron-beam induced deposition. Cross sections were imaged in bright-field and high angle annular dark-field scanning transmission electron microscopy (HAADF-STEM) modes. Energy-dispersive X-ray spectroscopy (EDS) was performed using this microscope (Figure 3).

Auger electron spectroscopy was performed at Stanford using a PHI-700 spectrometer. X-ray photoelectron spectroscopy (XPS) measurements were done at TU/e using Thermo Scientific KA1066 and at Stanford PHI Versaprobe III spectrometers with mono-
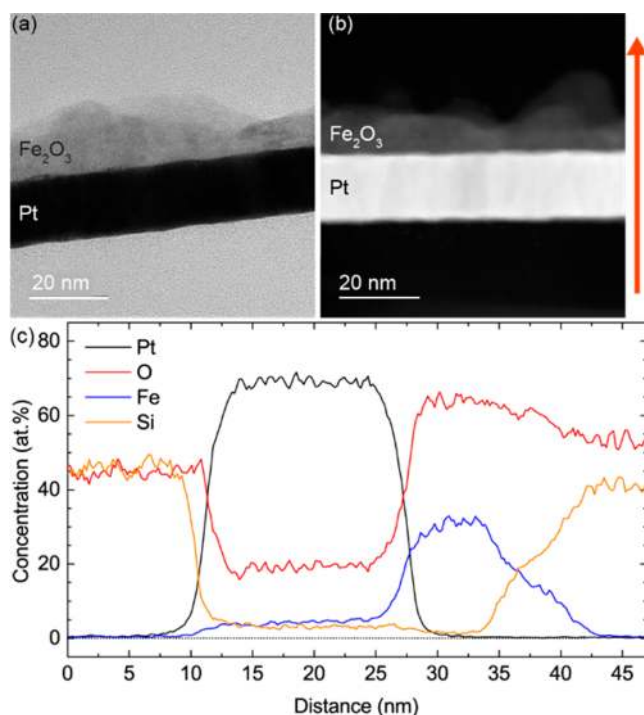


**Figure 3.** Cross-sectional TEM micrographs of Fe$_2$O$_3$ deposited on a Pt substrate as recorded using (a) bright-field TEM and (b) HAADF-STEM. (c) Elemental concentrations determined using EDS line scan in cross-sectional view, along the vertical direction as indicated by the arrow in (b). The elemental concentrations measured are averaged over a ∼ 40 nm lateral distance. The Si signal for distances > 33 nm results from the protective SiO$_2$ layer deposited prior to FIB milling.

chromatic Al K$\alpha$ X-rays in both cases, and using Ar$^+$ sputtering for depth profiling.

Core/shell Pt/Fe$_2$O$_3$ nanoparticles were deposited at Stanford by ALD on Aerosil OX50 silica powder, which was cleaned using UV irradiation and ozone. The powder was contained in a custom stainless steel cup with lid based on a design by Libera et al.[44] A standard Pt ALD process was used to deposit Pt nanoparticles with the Stanford Arradiance system.[45] Fe$_2$O$_3$ was deposited in the Stanford custom system using alternating exposures of TBF and O$_2$ gas, with the silica powder heated to 250 °C. To saturate the high surface area of the powder, for these experiments, cycles consisted of 10−15 s TBF exposure, followed by 20 s holding time, 120 s purge time, 1.5 s O$_2$ exposure, followed by 30 s holding time, and 120 s purge time.

TEM of the prepared nanoparticles was performed at Stanford using an FEI G2 F20 Tecnai TEM (Figure 6) and an FEI Titan environmental transmission electron microscope (Figure 7 and Figure S3). Scanning transmission electron microscopy (STEM) and energy-dispersive spectroscopy (EDS) were carried out on the Titan microscope. The SiO$_2$ nanospheres on which the nanoparticles were prepared were dropcast onto Cu TEM grids with lacey or ultrathin C.

■ **RESULTS**

**ALD Growth and Substrate Selectivity.** *In situ* SE was performed to characterize the selectivity and growth properties of the area-selective Fe$_2$O$_3$ process. Depositions were carried out on a number of different starting substrates to verify the need for a catalytically active film. The substrates include Pt, Au, Fe$_2$O$_3$, SiO$_2$, and Al$_2$O$_3$ (as described in the Methods section). Plots of the thickness as a function of cycle number are presented in Figure 2a for the Pt and Fe$_2$O$_3$ substrates, using various TBF exposure times. On the Pt substrates, growth of Fe$_2$O$_3$ is clearly observed. The growth rate increases during

the initial 100 cycles until a constant growth rate is achieved. This behavior is typical for the growth of polycrystalline films.[46] In the inset of Figure 2a, the saturation curve for the TBF exposure is shown as determined at 100 cycles or 250 cycles. At low film thicknesses up to ∼5 nm (around 100 cycles), the process appears to be in saturation after 10 s TBF exposure and reaches a growth rate of 0.045 nm/cycle. For thicker films at 250 cycles, however, the growth rate for 20 s TBF exposure (0.070 nm/cycle) is higher than for 10 s TBF exposure (0.057 nm/cycle), suggesting that the process is no longer in saturation. This observation will be explained in terms of a possible reaction mechanism in the Discussion section below. We note that the growth rate of 0.070 nm/cycle is similar to results observed for ALD using TBF and $O_2$ plasma.[42]

It is evident from the growth curves of Figure 2a that negligible growth occurs on as-deposited $Fe_2O_3$ substrates (with no Pt underneath, substrate "3" as described in the Methods section), with a growth rate of only 0.005 nm/cycle for 10 s TBF exposure. This is an important observation as it confirms that the $Fe_2O_3$ film itself is not catalyzing the deposition of additional $Fe_2O_3$.

Figure 2b shows XPS scans of the $Fe_{2p}$ region on the Pt, Au, $SiO_2$, and $Al_2O_3$ substrates after a deposition of 300 cycles. Fe is detected on the Pt substrate, with the Fe $2p_{3/2}$ peak located at 711.0 eV, in good agreement with Fe(III) in $Fe_2O_3$ (710.9 eV).[47] In addition, the spin orbit splitting between Fe $2p_{1/2}$ and Fe $2p_{3/2}$ is 13.6 eV as expected for Fe(III) in $Fe_2O_3$.[47] Prior work on ALD of $Fe_2O_3$ films using ferrocene precursors found that the films consisted of either $\alpha$-$Fe_2O_3$ or amorphous $Fe_2O_3$.[37,42,48,49] Furthermore, no Fe is detected after deposition on the Au, $SiO_2$, and $Al_2O_3$ substrates. These results demonstrate that the process has excellent selectivity, with immediate growth on Pt substrates (Figure 2a) and no indication of any growth on $SiO_2$ or $Al_2O_3$ substrates (Figure 2b). Furthermore, the lack of growth on Au substrates indicates that a metal catalytically active for $O_2$ dissociation, such as Pt or Ir, is required.

We also note another interesting observation: on Pt substrates, the $Fe_2O_3$ layer can deposit to at least 20 nm in thickness without noticeable attenuation of the growth rate. This is in contrast to the expectation that the growth will stop once the catalytic surface has been covered. This behavior is discussed in detail in the Discussion section.

**Microstructure and Composition.** Bright-field and dark-field cross-sectional TEM micrographs of a $Fe_2O_3$ film deposited with 300 $Fe_2O_3$ ALD cycles on a Pt substrate are provided in Figure 3. The $Fe_2O_3$ layer has completely covered the Pt substrate. However, the layer appears to be polycrystalline, resulting in grain boundaries and a high roughness. The images show a clearly defined interface between the underlying Pt substrate and the $Fe_2O_3$ film. Furthermore, Figure 3c shows the elemental concentrations as measured by EDS in the cross-sectional orientation. EDS likewise supports a clearly defined interface between the Pt and the $Fe_2O_3$ layers with no detectable Pt within the $Fe_2O_3$ layer. A plan-view scanning electron micrograph is shown in Figure S1, in which the polycrystallinity and resulting roughness is clearly visible.

The stoichiometry and chemical structure of $Fe_2O_3$ films on Pt substrates were investigated using XPS depth profiling by $Ar^+$ ion sputtering. Figure 4 shows the concentration of Pt, C, O, and Fe in a 17 nm $Fe_2O_3$ film as a function of the sputtering time (representing the depth). The initial surface measurement before any sputtering shows atomic concentrations of 60% O,
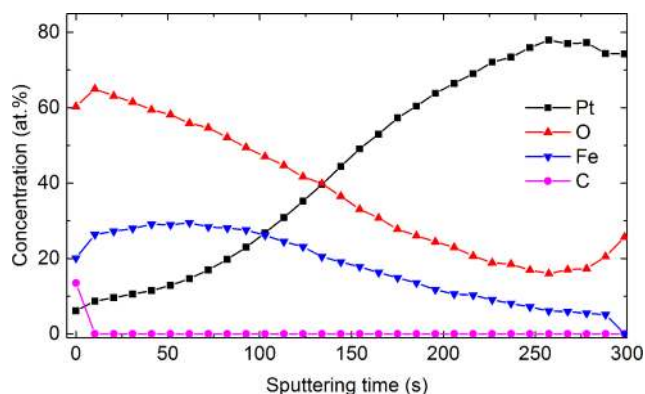


**Figure 4.** XPS sputter depth profile of a 17 nm thick $Fe_2O_3$ film on a Pt substrate.

20% Fe, 13% C (adventitious), and 6% Pt. Initially, the Fe concentration remains constant while there is a reduction in O concentration most likely resulting from preferential sputtering of O.[50] The small amount of C present on the surface is fully removed after the first sputtering cycle, indicating it is only present on the surface and is the result of adventitious C contamination. The detection of Pt in the initial surface measurement is likely caused by the probing of the underlying Pt film, and not from possible Pt in the $Fe_2O_3$ film itself. Due to the high roughness of the $Fe_2O_3$ film, there are some regions of the film where the thickness is low enough (∼10 nm) for XPS to detect the underlying substrate. The absence of significant Pt signal in the cross-sectional EDS measurement (Figure 3c) further supports that the 6% Pt originates from the substrate and not the $Fe_2O_3$ film itself.

**Selectivity on Patterned Samples.** We employed AES to investigate the selectivity of the deposition process on microstructured patterns. AES maps and line scans of $Fe_2O_3$ deposited on $SiO_2$ substrates with patterned Pt squares are presented in Figure 5. The high spatial correlation between Pt and Fe elemental signals in the AES maps further supports the
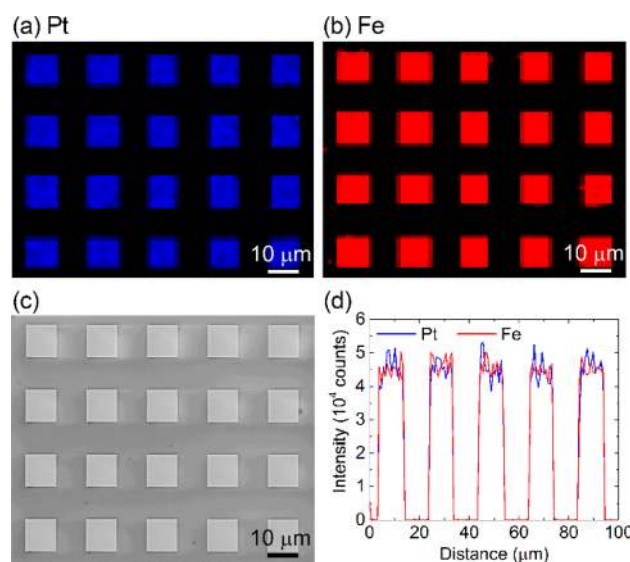


**Figure 5.** AES elemental maps for (a) Pt and (b) Fe of $Fe_2O_3$ deposited on patterned Pt substrates. (c) Corresponding SEM image. (d) Line scan showing Pt and Fe counts. The AES maps show excellent correlation between the Pt and Fe signals.

preference for deposition on Pt over $SiO_2$ surfaces. On the basis of the ratio of observed elemental counts in the Pt and $SiO_2$ regions of the substrate, the selectivity for deposition on Pt versus $SiO_2$ is 2000:1.

The area-selective deposition of NiO and $Fe_2O_3$ on $SiO_2$ substrates with patterned Ir was similarly investigated by AES, and the results are presented in Figure S2. There is also a very high correlation between the Fe and Ir, and likewise the Ni and Ir signals. Very low Ni and Fe levels are detected in the $SiO_2$ regions where Ir is not present, giving selectivities of 200:1 for Ni and 900:1 for Fe.

**Synthesis of Core–Shell Nanoparticles.** The area-selective ALD process reported here is ideal for the preparation of core/shell nanoparticles, as a metal oxide shell can be deposited selectively on catalytically active core particles. As a demonstration, we prepared core/shell $Pt/Fe_2O_3$ nanoparticles. The Pt core particles were deposited by performing 50 cycles of Pt ALD on a $SiO_2$ nanosphere support, and subsequently, the $Fe_2O_3$ shell was deposited using either 25 or 50 cycles of the area-selective $Fe_2O_3$ ALD process. Bright-field TEM micrographs of these nanoparticles are shown in Figure 6. The
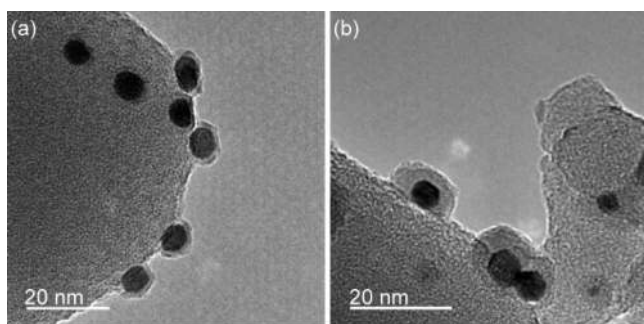


**Figure 6.** Bright-field TEM images of $Pt/Fe_2O_3$ core/shell nanoparticles supported on $SiO_2$ nanospheres prepared by 50 cycles of Pt ALD, followed by (a) 25 cycles and (b) 50 cycles of $Fe_2O_3$ ALD from $TBF/O_2$.

micrographs indicate a dark, strongly diffracting core with a lighter, weakly diffracting shell. The core is assigned to Pt and the shell to $Fe_2O_3$, as follows. Lattice fringes spaced by 0.23 Å in the dark core correspond to the Pt(111) crystal plane spacing. Strong lattice fringes are not observed in the shell, which may be due to limited crystallinity and the lower atomic number ($Z$) of Fe. Where fringes are observed, they are spaced by 0.27 Å corresponding closely to the $Fe_2O_3$(104) crystal plane spacing which agrees with the XPS results discussed above. As expected, the thickness of the $Fe_2O_3$ shell increases in going from 25 to 50 cycles. An annular dark-field (ADF) micrograph and a corresponding STEM-EDS line scan are shown in Figure 7. The dark-field image shows a strongly scattering core in each particle and a weakly scattering shell, which corresponds to a high Z Pt core and a low Z $Fe_2O_3$ shell. During the line scan (direction indicated in Figure 7a), the Fe signal appears before the Pt signal is observed, also in support of a core/shell structure with an Fe-containing shell and a Pt core. A STEM-EDS map and corresponding ADF micrograph are presented in Figure S3. In the elemental map, there is a high correlation between the Pt and Fe signals supporting area-selectivity. Very few Fe counts are observed in regions where only Si is present.
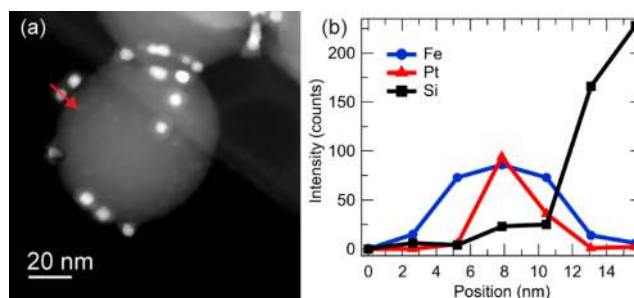


**Figure 7.** (a) ADF micrograph and (b) STEM-EDS line profile of $Pt/Fe_2O_3$ nanoparticles supported on $SiO_2$ prepared using 50 cycles of Pt ALD, followed by 50 cycles of $Fe_2O_3$ ALD from $TBF/O_2$. The large $SiO_2$ sphere is decorated with smaller Pt nanoparticles that in turn are coated with $Fe_2O_3$. The location and direction of the line scan in (b) is marked on the ADF micrograph in (a).

## DISCUSSION

The selective growth of $Fe_2O_3$ and NiO on Pt and Ir surfaces was demonstrated. No growth of $Fe_2O_3$ and NiO was observed on $SiO_2$, $Al_2O_3$, and Au surfaces. The mechanism of this deposition process will now be discussed.

We propose a reaction mechanism closely related to the mechanism for ALD of Pt-group metals, most notably the ALD process for Pt using $MeCpPtMe_3$ and $O_2$ gas which was demonstrated to involve the chemisorption of oxygen.[22,51] In each cycle of this Pt ALD process, oxygen dissociatively chemisorbs on the Pt surface during the oxygen half reaction, and the chemisorbed oxygen oxidizes the ligands from the $MeCpPtMe_3$ precursor. These combustion-like reactions happen during both the $MeCpPtMe_3$ and oxygen half-reactions.[52−54]

Similarly, we propose a mechanism (Figure 1) where, in each $Fe_2O_3$ or NiO ALD cycle, oxygen dissociatively chemisorbs during the oxygen half-reaction on the catalytic Pt or Ir substrate and not on surfaces inactive for oxygen activation (e.g., Au, $SiO_2$, $Fe_2O_3$, or $Al_2O_3$). On the catalytic Pt or Ir, dissociatively chemisorbed oxygen species then combust the ligands of the nickelocene and t-butyl ferrocene. The lack of chemisorbed oxygen on the inactive substrates is the reason why no deposition occurs on these surfaces. Importantly, the lack of growth on Au substrates supports the requirement of a catalytically active substrate for the growth, since Au films are not catalytically active toward oxygen dissociation (except in small Au clusters).[55−57]

In this mechanism, one might expect the growth of the transition metal oxide to attenuate when the catalytically active substrate becomes covered by the growing metal oxide film. However, in the case of $Fe_2O_3$ on Pt shown in Figure 2, linear growth is sustained for at least 300 cycles (resulting in >20 nm growth), at which point the Pt substrate is already fully covered by $Fe_2O_3$ (as can be concluded from TEM images; see Figure 3). Figure 2a also shows that the growth is almost negligible on $Fe_2O_3$ substrates, where the initial $Fe_2O_3$ film is grown using nonselective ALD with $TBF/O_2$ plasma. This indicates that the $Fe_2O_3$ material itself does not provide a significant catalytic contribution to the growth.

The mechanism of the sustained growth is currently not fully understood. One key hypothesis is that, during the oxygen half-reaction, oxygen diffuses into the $Fe_2O_3$ film, reaches the Pt substrate, and is dissociated there. This diffusion is likely enhanced by the presence of grain boundaries resulting from

the polycrystalline nature of the film as seen in Figure 3 and Figure S1. If the dissociated O* can diffuse back toward the surface, it could react with the TBF precursor during the subsequent precursor half-cycle. In this way, the $Fe_2O_3$ film could act as a reservoir for oxygen. A similar phenomenon was observed during $SiO_2$ ALD on Ag, where $Ag_2O$ is formed and releases O species, resulting in increased $SiO_2$ deposition.[58] The saturation behavior of our process as shown in the inset of Figure 2a provides some evidence for this mechanism. For thin $Fe_2O_3$ films up to 100 cycles, saturated growth is observed. In contrast, however, for thicker films such as at 250 cycles, the growth rate increases going from 10 to 20 s of TBF exposure. This supports the proposed mechanism, as thicker $Fe_2O_3$ films would have a higher oxygen uptake capacity, allowing for increased amounts of oxygen to be released. Consequently, a higher TBF dose would be required for the growth to saturate. We expect saturation to eventually occur if the TBF exposure time is increased.

An alternative explanation may be the presence of a small amount of Pt in or on the $Fe_2O_3$ film. Diffusion of Pt from the substrate toward the top of the $Fe_2O_3$ layer may be possible at the elevated growth temperature, and this Pt may be catalyzing the growth. However, no Pt is detected in the $Fe_2O_3$ layer in the cross-sectional EDS measurement (Figure 3c), which makes this explanation less likely. As mentioned previously, the observation of Pt in the XPS depth profiling (Figure 4) is likely due to detection of the Pt substrate through thinner regions of the $Fe_2O_3$ film. Therefore, we do not expect surface Pt species to play a key role in the continued growth; however, we cannot conclusively rule out the presence of trace amounts of Pt below the EDS detection limit.

The process of area-selective ALD that we demonstrate here should be extendable to a variety of systems. First, we have shown that selectivity can be achieved for two different transition metal oxide ALD systems ($Fe_2O_3$ and NiO) on two different catalytic substrates (Pt and Ir). Moreover, the ability to perform these selective depositions in ALD reactors of different designs and on both flat and nanoparticle substrates supports the robustness of our processes. By using Pt-group metal surfaces such as Pt, Ir, Pd, and Ru as the substrate to catalyze the oxidant reaction, we expect that area-selective deposition can be achieved through a similar mechanism for almost any metal oxide ALD system that uses a precursor requiring a strong oxidizing agent for growth (i.e., does not react with molecular $O_2$) such as $Co_3O_4$,[59] $In_2O_3$,[60] and $MoO_3$.[61] Likewise, there are other materials that can chemisorb and catalyze oxygen dissociation, and this may allow for selective growth even on non-noble metals such as Cu.[62] Furthermore, similar mechanisms may be possible with other co-reactants such as hydrogen,[8] as demonstrated by the selective deposition of Pd on Pt particles via hydrogen dissociation.[16]

## CONCLUSIONS

We studied the area-selective ALD of $Fe_2O_3$ and NiO on Pt and Ir surfaces, using t-butyl ferrocene and nickelocene precursors, which conventionally require strong oxidizing agents. When using molecular $O_2$ gas as the co-reactant, ALD growth can only be obtained on catalytically active surfaces, a phenomenon that was exploited for achieving area-selective ALD. These substrates catalyze dissociative chemisorption of $O_2$, leading to activated O* that participates in the ALD reactions, while no growth occurs on substrates that do not possess catalytic

activity for $O_2$ dissociation including Au, $SiO_2$, and $Al_2O_3$. Area-selective deposition is thereby achieved through the catalytic activity of the underlying substrate.

Process characterization was performed using in situ spectroscopic ellipsometry. XPS measurements on Au, $SiO_2$, and $Al_2O_3$ show no indication of any Fe presence after 300 ALD cycles of $Fe_2O_3$ ALD, which confirms the high selectivity of the process. Area-selective ALD was demonstrated by successfully depositing $Fe_2O_3$ and NiO on micron-scale Pt and Ir patterns. AES measurements on these patterned samples yielded selectivity values of 2000:1 for $Fe_2O_3$ on Pt with respect to $SiO_2$, and 200:1 for NiO on Ir. Furthermore, Pt/$Fe_2O_3$ core/shell nanoparticles were synthesized by performing area-selective ALD of $Fe_2O_3$ on Pt nanoparticles.

Finally, the demonstrated area-selective deposition of both $Fe_2O_3$ and NiO, as well as the similarity of results obtained in different reactors, supports the robustness of the process. This approach holds promise for the area-selective deposition of a wide range of other metal oxides for which the precursor does not react with molecular oxygen, for example, processes relying on $O_2$ plasma or ozone as co-reactant. In particular, the Fe/Pt-based results may be applied for preparation of magnetic or spintronic devices, or catalyst particles for the synthesis of carbon nanotubes.

## ■ ASSOCIATED CONTENT

### Ⓢ Supporting Information
The Supporting Information is available free of charge on the ACS Publications website at DOI: 10.1021/acs.chemmater.7b03818.

SEM micrograph of $Fe_2O_3$/Pt, AES lines scans on Ir, and STEM-EDS mapping of $Fe_2O_3$/Pt (PDF)

## ■ AUTHOR INFORMATION

### Corresponding Authors
*E-mail: a.j.m.mackus@tue.nl (A.J.M.M.).
*E-mail: sbent@stanford.edu (S.F.B.).

### ORCID ⊕
Joseph A. Singh: 0000-0001-5249-2121
Wilhelmus M. M. Kessels: 0000-0002-7630-8226
Ageeth A. Bol: 0000-0002-1259-6265
Stacey F. Bent: 0000-0002-1084-5336
Adriaan J. M. Mackus: 0000-0001-6944-9867

### Author Contributions
#These authors contributed equally. The manuscript was written through contributions of all authors. All authors have given approval to the final version of the manuscript.

### Notes
The authors declare no competing financial interest.

## ■ ACKNOWLEDGMENTS

## ■ REFERENCES

(1) Mackus, A. J. M.; Bol, A. A.; Kessels, W. M. M. The Use of Atomic Layer Deposition in Advanced Nanopatterning. *Nanoscale* **2014**, *6* (19), 10941−10960.

(2) Lee, H.-B.-R.; Bent, S. F. Nanopatterning by Area-Selective Atomic Layer Deposition. In *Atomic Layer Deposition of Nanostructured Materials*; Wiley-VCH Verlag GmbH & Co. KGaA: Weinheim, Germany, 2012; pp 193−225.

(3) Singh, J. A.; Yang, N.; Bent, S. F. Nanoengineering Heterogeneous Catalysts by Atomic Layer Deposition. *Annu. Rev. Chem. Biomol. Eng.* **2017**, *8* (1), 41−62.

(4) O'Neill, B. J.; Jackson, D. H. K.; Lee, J.; Canlas, C.; Stair, P. C.; Marshall, C. L.; Elam, J. W.; Kuech, T. F.; Dumesic, J. A.; Huber, G. W. Catalyst Design with Atomic Layer Deposition. *ACS Catal.* **2015**, *5* (3), 1804−1825.

(5) Wrobleski, J. T.; Boudart, M. Preparation of Solid Catalysts: An Appraisal. *Catal. Today* **1992**, *15* (3−4), 349−360.

(6) Ferrando, R.; Jellinek, J.; Johnston, R. L. Nanoalloys: From Theory to Applications of Alloy Clusters and Nanoparticles. *Chem. Rev.* **2008**, *108* (3), 845−910.

(7) Hutchings, G. J.; Kiely, C. J. Strategies for the Synthesis of Supported Gold Palladium Nanoparticles with Controlled Morphology and Composition. *Acc. Chem. Res.* **2013**, *46* (8), 1759−1772.

(8) Lu, J.; Low, K.-B.; Lei, Y.; Libera, J. A.; Nicholls, A.; Stair, P. C.; Elam, J. W. Toward Atomically-Precise Synthesis of Supported Bimetallic Nanoparticles Using Atomic Layer Deposition. *Nat. Commun.* **2014**, *5*, 3264.

(9) Longo, R. C.; McDonnell, S.; Dick, D.; Wallace, R. M.; Chabal, Y. J.; Owen, J. H. G.; Ballard, J. B.; Randall, J. N.; Cho, K. Selectivity of Metal Oxide Atomic Layer Deposition on Hydrogen Terminated and Oxidized Si(001)-(2 × 1) Surface. *J. Vac. Sci. Technol., B: Nanotechnol. Microelectron.: Mater., Process., Meas., Phenom.* **2014**, *32*, 03D112.

(10) Hashemi, F. S. M.; Prasittichai, C.; Bent, S. F. A New Resist for Area Selective Atomic and Molecular Layer Deposition on Metal−Dielectric Patterns. *J. Phys. Chem. C* **2014**, *118* (20), 10957−10962.

(11) Fang, M.; Ho, J. C. Area-Selective Atomic Layer Deposition: Conformal Coating, Subnanometer Thickness Control, and Smart Positioning. *ACS Nano* **2015**, *9* (9), 8651−8654.

(12) Moshe, H.; Mastai, Y. Atomic Layer Deposition on Self-Assembled-Monolayers. In *Materials Science - Advanced Topics*; InTech: London, 2013; Chapter 3, pp 63−84.

(13) Cao, K.; Zhu, Q.; Shan, B.; Chen, R. Controlled Synthesis of Pd/Pt Core Shell Nanoparticles Using Area-Selective Atomic Layer Deposition. *Sci. Rep.* **2015**, *5*, 8470.

(14) Avila, J. R.; DeMarco, E. J.; Emery, J. D.; Farha, O. K.; Pellin, M. J.; Hupp, J. T.; Martinson, A. B. F. Real-Time Observation of Atomic Layer Deposition Inhibition: Metal Oxide Growth on Self-Assembled Alkanethiols. *ACS Appl. Mater. Interfaces* **2014**, *6* (15), 11891−11898.

(15) Sampson, M. D.; Emery, J. D.; Pellin, M. J.; Martinson, A. B. F. Inhibiting Metal Oxide Atomic Layer Deposition: Beyond Zinc Oxide. *ACS Appl. Mater. Interfaces* **2017**, *9* (39), 33429−33436.

(16) Weber, M. J.; Mackus, A. J. M.; Verheijen, M. A.; van der Marel, C.; Kessels, W. M. M. Supported Core/Shell Bimetallic Nanoparticles Synthesis by Atomic Layer Deposition. *Chem. Mater.* **2012**, *fe224* (15), 2973−2977.

(17) Wang, H.; Wang, C.; Yan, H.; Yi, H.; Lu, J. Precisely-Controlled Synthesis of Au@Pd Core-Shell Bimetallic Catalyst via Atomic Layer Deposition for Selective Oxidation of Benzyl Alcohol. *J. Catal.* **2015**, *324*, 59−68.

(18) Weber, M. J.; Verheijen, M. A.; Bol, A. A.; Kessels, W. M. M. Sub-Nanometer Dimensions Control of Core/shell Nanoparticles Prepared by Atomic Layer Deposition. *Nanotechnology* **2015**, *26* (9), 094002.

(19) Vallat, R.; Gassilloud, R.; Eychenne, B.; Vallée, C. Selective Deposition of Ta$_2$O$_5$ by Adding Plasma Etching Super-Cycles in Plasma Enhanced Atomic Layer Deposition Steps. *J. Vac. Sci. Technol., A* **2017**, *35* (1), 01B104.

(20) Hashemi, F. S. M.; Prasittichai, C.; Bent, S. F. Self-Correcting Process for High Quality Patterning by Atomic Layer Deposition. *ACS Nano* **2015**, *9* (9), 8710−8717.

(21) Lu, J.; Elam, J. W.; Stair, P. C. Atomic Layer deposition—Sequential Self-Limiting Surface Reactions for Advanced Catalyst "bottom-Up" Synthesis. *Surf. Sci. Rep.* **2016**, *71* (2), 410−472.

(22) MacKus, A. J. M.; Leick, N.; Baker, L.; Kessels, W. M. M. Catalytic Combustion and Dehydrogenation Reactions during Atomic Layer Deposition of Platinum. *Chem. Mater.* **2012**, *24* (10), 1752−1761.

(23) Li, S. S.; Hou, P. X.; Liu, C.; Gao, L. B.; Liu, B. L.; Zhang, L. L.; Song, M.; Cheng, H. M. Wall-Number Selective Growth of Vertically Aligned Carbon Nanotubes from FePt Catalysts: A Comparative Study with Fe Catalysts. *J. Mater. Chem.* **2012**, *22* (28), 14149−14154.

(24) He, M.; Jin, H.; Zhang, L.; Jiang, H.; Yang, T.; Cui, H.; Fossard, F.; Wagner, J. B.; Karppinen, M.; Kauppinen, E. I.; Loiseau, A. Environmental Transmission Electron Microscopy Investigations of Pt-Fe$_2$O$_3$Nanoparticles for Nucleating Carbon Nanotubes. *Carbon* **2016**, *110*, 243−248.

(25) Enterkin, J. A.; Poeppelmeier, K. R.; Marks, L. D. Oriented Catalytic Platinum Nanoparticles on High Surface Area Strontium Titanate Nanocuboids. *Nano Lett.* **2011**, *11* (3), 993−997.

(26) Ohashi, T.; Shima, T. Synthesis of Vertically Aligned Single-Walled Carbon Nanotubes with Metallic Chirality through Facet Control of Catalysts. *Carbon* **2015**, *87* (C), 453−461.

(27) Stamenkovic, V. R.; Mun, B. S.; Arenz, M.; Mayrhofer, K. J. J.; Lucas, C. A.; Wang, G.; Ross, P. N.; Markovic, N. M. Trends in Electrocatalysis on Extended and Nanoscale Pt-Bimetallic Alloy Surfaces. *Nat. Mater.* **2007**, *6* (3), 241−247.

(28) Zhu, H.; Wu, Z.; Su, D.; Veith, G. M.; Lu, H.; Zhang, P.; Chai, S.-H.; Dai, S. Constructing Hierarchical Interfaces: TiO$_2$ -Supported PtFe—FeO$_x$ Nanowires for Room Temperature CO Oxidation. *J. Am. Chem. Soc.* **2015**, *137* (32), 10156−10159.

(29) Camacho-Bunquin, J.; Shou, H.; Aich, P.; Beaulieu, D. R.; Klotzsch, H.; Bachman, S.; Marshall, C. L.; Hock, A.; Stair, P. Catalyst Synthesis and Evaluation Using an Integrated Atomic Layer Deposition Synthesis−catalysis Testing Tool. *Rev. Sci. Instrum.* **2015**, *86* (8), 084103.

(30) Gould, T. D.; Montemore, M. M.; Lubers, A. M.; Ellis, L. D.; Weimer, A. W.; Falconer, J. L.; Medlin, J. W. Enhanced Dry Reforming of Methane on Ni and Ni-Pt Catalysts Synthesized by Atomic Layer Deposition. *Appl. Catal., A* **2015**, *492*, 107−116.

(31) Ramachandran, R. K.; Detavernier, C.; Dendooven, J. Atomic Layer Deposition for Catalysis. In *Nanotechnology in Catalysis*; Wiley-VCH Verlag GmbH & Co. KGaA: Weinheim, Germany, 2017; pp 335−358.

(32) Johansson, A.-C.; Larsen, J. V.; Verheijen, M. A.; Haugshøj, K. B.; Clausen, H. F.; Kessels, W. M. M.; Christensen, L. H.; Thomsen, E. V. Electrocatalytic Activity of Atomic Layer Deposited Pt—Ru Catalysts onto N-Doped Carbon Nanotubes. *J. Catal.* **2014**, *311*, 481−486.

(33) Sun, S. Monodisperse FePt Nanoparticles and Ferromagnetic FePt Nanocrystal Superlattices. *Science* **2000**, *287* (5460), 1989−1992.

(34) Hyeon, T. Chemical Synthesis of Magnetic Nanoparticles. *Chem. Commun.* **2003**, 927−934.

(35) Feng, C.; Zhao, J.; Yang, F.; Gong, K.; Hao, S.; Cao, Y.; Hu, C.; Zhang, J.; Wang, Z.; Chen, L.; Li, S.; Sun, L.; Cui, L.; Yu, G. Nonvolatile Modulation of Electronic Structure and Correlative

Magnetism of L10-FePt Films Using Significant Strain Induced by Shape Memory Substrates. *Sci. Rep.* **2016**, *6*, 20199.

(36) Taylor, R. M.; Huber, D. L.; Monson, T. C.; Ali, A.-M. S.; Bisoffi, M.; Sillerud, L. O. Multifunctional Iron Platinum Stealth Immunomicelles: Targeted Detection of Human Prostate Cancer Cells Using Both Fluorescence and Magnetic Resonance Imaging. *J. Nanopart. Res.* **2011**, *13* (10), 4717–4729.

(37) Martinson, A. B. F.; DeVries, M. J.; Libera, J. A.; Christensen, S. T.; Hupp, J. T.; Pellin, M. J.; Elam, J. W. Atomic Layer Deposition of $Fe_2O_3$ Using Ferrocene and Ozone. *J. Phys. Chem. C* **2011**, *115* (10), 4333–4339.

(38) Bachmann, J.; Zolotaryov, A.; Albrecht, O.; Goetze, S.; Berger, A.; Hesse, D.; Novikov, D.; Nielsch, K. Stoichiometry of Nickel Oxide Films Prepared by ALD. *Chem. Vap. Deposition* **2011**, *17* (7–9), 177–180.

(39) Heil, S. B. S.; Langereis, E.; Roozeboom, F.; van de Sanden, M. C. M.; Kessels, W. M. M. Low-Temperature Deposition of TiN by Plasma-Assisted Atomic Layer Deposition. *J. Electrochem. Soc.* **2006**, *153* (11), G956–G965.

(40) Faraz, T.; van Drunen, M.; Knoops, H. C. M.; Mallikarjunan, A.; Buchanan, I.; Hausmann, D. M.; Henri, J.; Kessels, W. M. M. Atomic Layer Deposition of Wet-Etch Resistant Silicon Nitride Using Di(*Sec*-Butylamino)silane and $N_2$ Plasma on Planar and 3D Substrate Topographies. *ACS Appl. Mater. Interfaces* **2017**, *9* (2), 1858–1869.

(41) Mackus, A. J. M.; Garcia-Alonso, D.; Knoops, H. C. M.; Bol, A. A.; Kessels, W. M. M. Room-Temperature Atomic Layer Deposition of Platinum. *Chem. Mater.* **2013**, *25* (9), 1769–1774.

(42) Ramachandran, R. K.; Dendooven, J.; Detavernier, C. Plasma Enhanced Atomic Layer Deposition of $Fe_2O_3$ Thin Films. *J. Mater. Chem. A* **2014**, *2* (27), 10662–10667.

(43) Langereis, E.; Heil, S. B. S.; Knoops, H. C. M.; Keuning, W.; van de Sanden, M. C. M.; Kessels, W. M. M. In Situ Spectroscopic Ellipsometry as a Versatile Tool for Studying Atomic Layer Deposition. *J. Phys. D: Appl. Phys.* **2009**, *42*, 073001–073019.

(44) Libera, J. A.; Elam, J. W.; Pellin, M. J. Conformal ZnO Coatings on High Surface Area Silica Gel Using Atomic Layer Deposition. *Thin Solid Films* **2008**, *516* (18), 6158–6166.

(45) Dai, P.; Xie, J.; Mayer, M. T.; Yang, X.; Zhan, J.; Wang, D. Solar Hydrogen Generation by Silicon Nanowires Modified with Platinum Nanoparticle Catalysts by Atomic Layer Deposition. *Angew. Chem., Int. Ed.* **2013**, *52* (42), 11119–11123.

(46) Nilsen, O.; Karlsen, O. B.; Kjekshus, A.; Fjellvåg, H. Simulation of Growth Dynamics in Atomic Layer Deposition. Part II. Polycrystalline Films from Cubic Crystallites. *Thin Solid Films* **2007**, *515* (11), 4538–4549.

(47) Biesinger, M. C.; Payne, B. P.; Grosvenor, A. P.; Lau, L. W. M.; Gerson, A. R.; Smart, R. S. C. Resolving Surface Chemical States in XPS Analysis of First Row Transition Metals, Oxides and Hydroxides: Cr, Mn, Fe, Co and Ni. *Appl. Surf. Sci.* **2011**, *257* (7), 2717–2730.

(48) Scheffe, J. R.; Francés, A.; King, D. M.; Liang, X.; Branch, B. A.; Cavanagh, A. S.; George, S. M.; Weimer, A. W. Atomic Layer Deposition of iron(III) Oxide on Zirconia Nanoparticles in a Fluidized Bed Reactor Using Ferrocene and Oxygen. *Thin Solid Films* **2009**, *517* (6), 1874–1879.

(49) Rooth, M.; Johansson, A.; Kukli, K.; Aarik, J.; Boman, M.; Harsta, A. Atomic Layer Deposition of Iron Oxide Thin Films and Nanotubes Using Ferrocene and Oxygen as Precursors. *Chem. Vap. Deposition* **2008**, *14* (3–4), 67–70.

(50) Mitchell, D. F.; Sproule, G. I.; Graham, M. J. Sputter Reduction of Oxides by Ion Bombardment during Auger Depth Profile Analysis. *Surf. Interface Anal.* **1990**, *15* (8), 487–497.

(51) Mackus, A. J. M.; Mulders, J. J. L.; van de Sanden, M. C. M.; Kessels, W. M. M. Local Deposition of High-Purity Pt Nanostructures by Combining Electron Beam Induced Deposition and Atomic Layer Deposition. *J. Appl. Phys.* **2010**, *107* (11), 116102.

(52) Kessels, W. M. M.; Knoops, H. C. M.; Dielissen, S. A. F.; Mackus, A. J. M.; van de Sanden, M. C. M. Surface Reactions during Atomic Layer Deposition of Pt Derived from Gas Phase Infrared Spectroscopy. *Appl. Phys. Lett.* **2009**, *95* (1), 013114.

(53) Aaltonen, T.; Rahtu, A.; Ritala, M.; Leskelä, M. Reaction Mechanism Studies on Atomic Layer Deposition of Ruthenium and Platinum. *Electrochem. Solid-State Lett.* **2003**, *6* (9), C130–C133.

(54) Mackus, A. J. M.; Thissen, N. F. W.; Mulders, J. J. L.; Trompenaars, P. H. F.; Verheijen, M. A.; Bol, A. A.; Kessels, W. M. M. Direct-Write Atomic Layer Deposition of High-Quality Pt Nanostructures: Selective Growth Conditions and Seed Layer Requirements. *J. Phys. Chem. C* **2013**, *117* (20), 10788–10798.

(55) Roldán, A.; González, S.; Ricart, J. M.; Illas, F. Critical Size for $O_2$ Dissociation by Au Nanoparticles. *ChemPhysChem* **2009**, *10* (2), 348–351.

(56) Haruta, M. Size- and Support-Dependency in the Catalysis of Gold. *Catal. Today* **1997**, *36* (1), 153–166.

(57) Lyalin, A.; Taketsugu, T. Reactant-Promoted Oxygen Dissociation on Gold Clusters. *J. Phys. Chem. Lett.* **2010**, *1* (12), 1752–1757.

(58) Ziegler, M.; Yüksel, S.; Goerke, S.; Weber, K.; Cialla-May, D.; Popp, J.; Pollok, K.; Wang, D.; Langenhorst, F.; Hübner, U.; Schaaf, P.; Meyer, H.-G. Growth of Hierarchically 3D Silver-Silica Hybrid Nanostructures by Metastable State Assisted Atomic Layer Deposition (MS-ALD). *Adv. Mater. Technol.* **2017**, *2*, 1700015.

(59) Donders, M. E.; Knoops, H. C. M.; Van, M. C. M.; Kessels, W. M. M.; Notten, P. H. L. Remote Plasma Atomic Layer Deposition of $Co_3O_4$ Thin Films. *J. Electrochem. Soc.* **2011**, *158* (4), G92–G96.

(60) Mane, A. U.; Allen, A. J.; Kanjolia, R. K.; Elam, J. W. Indium Oxide Thin Films by Atomic Layer Deposition Using Trimethylindium and Ozone. *J. Phys. Chem. C* **2016**, *120* (18), 9874–9883.

(61) Vos, M. F. J.; Macco, B.; Thissen, N. F. W.; Bol, A. A.; Kessels, W. M. M. Atomic Layer Deposition of Molybdenum Oxide from $(NtBu)_2(NMe_2)_2Mo$ and $O_2$ Plasma. *J. Vac. Sci. Technol., A* **2016**, *34* (1), 01A103.

(62) López-Moreno, S.; Romero, A. H. Atomic and Molecular Oxygen Adsorbed on (111) Transition Metal Surfaces: Cu and Ni. *J. Chem. Phys.* **2015**, *142* (15), 154702.